

# Observability of the virialization phase of spheroidal galaxies with radio arrays

M. Massardi,<sup>1,2★</sup> A. Lapi,<sup>1,3</sup> G. De Zotti,<sup>1,4</sup> R. D. Ekers<sup>2</sup> and L. Danese<sup>1</sup>

<sup>1</sup>SISSA–ISAS, Via Beirut 2-4, Trieste, Italy

<sup>2</sup>Australia Telescope National Facility, CSIRO, PO Box 76, Epping, NSW 1710, Australia

<sup>3</sup>Dip. Fisica, Univ. ‘Tor Vergata’, Via Ricerca Scientifica 1, 00133 Roma, Italy

<sup>4</sup>INAF, Osservatorio Astronomico di Padova, Vicolo dell’Osservatorio 5, I-35122 Padova, Italy

Accepted 2007 November 15. Received 2007 November 13; in original form 2007 June 22

## ABSTRACT

In the standard galaxy formation scenario plasma clouds with a high thermal energy content must exist at high redshifts since the protogalactic gas is shock heated to the virial temperature, and extensive cooling, leading to efficient star formation, must await the collapse of massive haloes (as indicated by the massive body of evidence, referred to as *downsizing*). Massive plasma clouds are potentially observable through the thermal and kinetic Sunyaev–Zel’dovich effects and their free–free emission. We find that the detection of substantial numbers of galaxy-scale thermal Sunyaev–Zel’dovich signals is achievable by blind surveys with next generation radio telescope arrays such as EVLA, ALMA and SKA. This population is even detectable with the 10 per cent SKA, and wide field of view options at high frequency on any of these arrays would greatly increase survey speed. An analysis of confusion effects and of the contamination by radio and dust emissions shows that the optimal frequencies are those in the range 10–35 GHz. Predictions for the redshift distributions of detected sources are also worked out.

**Key words:** instrumentation: interferometers – galaxies: formation – galaxies: high-redshift.

## 1 INTRODUCTION

A satisfactory theory of galaxy formation requires a good understanding of the complex physical processes governing the collapse of primordial density perturbations and the early galaxy evolution. Measurements of the galaxy luminosity and stellar mass functions up to substantial redshifts have highlighted that these functions show conspicuous differences with respect to the halo mass functions predicted by the cold dark matter (CDM) theory with the ‘concordance’ cosmological parameters. At the low-mass end, the halo mass functions are much steeper than the galaxy luminosity function. As discussed by many authors (Larson 1974; Dekel & Silk 1986; Cole 1991; Lacey & Silk 1991; White & Frenk 1991; Kauffmann, White & Guiderdoni 1993; Cole et al. 1994; Somerville & Primack 1999; Granato et al. 2001; Benson et al. 2003), the relative paucity of low-luminosity galaxies may be attributed to the quenching of star formation in low-mass haloes by energy injections from supernovae (SNe) and stellar winds, and by photoionization of the pre-galactic gas. This leads to the conclusion that efficient star formation must await the collapse of massive haloes. On the other hand, the above processes have little effect on very massive haloes, which, in the absence of additional relieving mechanisms, would convert too large fractions of gas into stars, yielding too many bright galaxies, with

wrong metallicities (Thomas, Maraston & Bender 2002; see Benson et al. 2003; Cirasuolo et al. 2005 for discussions of the effect of quenching mechanisms). An effective cure for that is the feedback from active galactic nuclei (AGN), growing at the galaxy centres (Granato et al. 2001, 2004; Bower et al. 2006; Croton et al. 2006).<sup>1</sup>

During their very early evolutionary phases, massive protogalaxies are expected to contain large amounts of hot gas, but the gas thermal history is obscure. According to the standard scenario (Rees & Ostriker 1977; White & Rees 1978), the protogalactic gas is shock heated to the virial temperature, but this view has been questioned (Birnbom & Dekel 2003; Katz et al. 2003; Binney 2004; Kereš et al. 2005), on the basis of independent approaches: analytic methods, a high-resolution one-dimensional code, smoothed particle hydrodynamics simulations. The general conclusion is that only a fraction, increasing with halo mass, of the gas heats to the virial temperature. The hot gas is further heated by SN explosions and by the AGN feedback, and may eventually be pushed out of the halo. Kereš et al. (2005) and Dekel & Birnbom (2006) find that there is a critical shock heating halo mass of  $\sim 10^{11.4}–10^{12} M_{\odot}$ , above which most

<sup>1</sup> Note that the AGN feedback invoked by Granato et al. is radically different from that advocated by Bower et al. and Croton et al. The former is a property of all AGN and is attributed to a combination of radiation pressure (especially line acceleration) and gas pressure. The latter is associated to the radio active phase of quasars (‘radio mode’ feedback).

★E-mail: massardi@sissa.it

of the gas is heated to the virial temperature, while most of the gas accreted by less massive haloes is cooler.

The large thermal energy content of the hot protogalactic gas in massive haloes makes this crucial evolutionary phase potentially observable by the next generation of astronomical instruments through its free–free emission and the thermal and kinetic SZ (tSZ and kSZ, respectively) effects (Oh 1999; Majumdar, Nath & Chiba 2001; Platania et al. 2002; Oh, Cooray & Kamionkowski 2003; de Zotti et al. 2004; Rosa-González et al. 2004). In this paper we investigate the detectability of this protogalactic gas exploiting an up-to-date model. For the purposes of the present analysis, the adopted model can be taken as representative of the most popular semi-analytic models (White & Frenk 1991; Kauffmann et al. 1993; Cole et al. 1994; Somerville & Primack 1999; Benson et al. 2003), that all adopt a similar mass function of dark matter (DM) haloes, a cosmological gas to DM ratio at virialization, and assume that all the gas is heated to the virial temperature.

Even if some single dish telescopes have the required theoretical sensitivity, especially at millimetre and submillimetre wavelengths (e.g. LMT/GTM, GBT at 3 mm, Rosa-González et al. 2004) these continuum observations will be hampered by fluctuations in tropospheric emission. Interferometric array observations offer a better trade off between angular resolution, sensitivity and control of systematics (Birkinshaw & Lancaster 2005) together with larger fields of view, and allow us to work at lower frequencies where the sources of contaminations from backgrounds and foregrounds are lower and may be better estimated. For this reason we focus mainly on the capabilities of next generation interferometers: the Square Kilometre Array (SKA),<sup>2</sup> the Atacama Large Millimetre Array (ALMA),<sup>3</sup> the Expanded Very Large Array (EVLA),<sup>4</sup> the new 7-mm capability of the Australia Telescope Compact Array (ATCA). We note that the situation for galaxy-scale SZ detection is quite different from that for cluster SZ detection. Cluster SZ signals are stronger and have much larger angular scales than optimum for the interferometer arrays and are best observed with single dishes at high-quality sites (Carlstrom, Holder & Reese 2002).

The outline of the paper is the following. In Section 2 we briefly describe our reference model; in Section 3, we present our predictions for the counts of protogalaxies seen through their free–free emission and their tSZ and kSZ effects; in Section 4 we analyse the potential of the next generation interferometers for detecting such signals, describe possible survey strategies, and discuss possible contaminating emissions and confusion effects; in Section 5, we summarize our main conclusions.

We adopt a  $\Lambda$ CDM cosmology with  $h = 0.71$ ,  $\Omega_m = 0.27$ ,  $\Omega_\lambda = 0.73$ ,  $\Omega_b = 0.04$ ,  $\sigma_8 = 0.8$ , consistent with the results from the *Wilkinson Microwave Anisotropy Probe* (Spergel et al. 2007).

## 2 OUTLINE OF THE MODEL

We adopt the semi-analytic model laid out in Granato et al. (2004), with the values of the parameters revised by Lapi et al. (2006) to satisfy the constraints set by the AGN luminosity functions. For the reader's convenience, we summarize here its main features.

The model is built in the framework of the standard hierarchical clustering scenario, taking also into account the results by Wechsler et al. (2002) and Zhao et al. (2003a,b), whose simulations have

shown that the growth of a halo occurs in two different phases: a first regime of fast accretion in which the potential well is built up by the sudden mergers of many clumps with comparable masses; and a second regime of slow accretion in which mass is added in the outskirts of the halo, without affecting the central region where the galactic structure resides. This means that the haloes harbouring a massive galaxy, once created even at high redshift, are rarely destroyed. At low redshifts they are incorporated within groups and clusters of galaxies. Support to this view comes from studies of the mass structure of elliptical galaxies, which are found not to show strong signs of evolution since redshift  $z \approx 1$  (Koopmans et al. 2006). The halo formation rate at  $z \gtrsim 1.5$ , when most massive early-type galaxies formed (Renzini 2006), is well approximated by the positive term in the cosmic time derivative of the cosmological mass function (e.g. Haehnelt & Rees 1993; Sasaki 1994).

We confine our analysis to galaxy halo masses between  $M_{\text{vir}}^{\text{min}} \approx 2.5 \times 10^{11} M_\odot$ , close to the mass scale at the boundary between the blue (low-mass, late-type) and the red (massive, early-type) galaxy sequences (Dekel & Birnboim 2006) and  $M_{\text{vir}}^{\text{max}} \approx 10^{13.2} M_\odot$ , the observational upper limit to halo masses associated to individual galaxies (Cirasuolo et al. 2005).

The complex physics of baryons is described by a set of equations summarized in the appendix of Lapi et al. (2006). Briefly, the model assumes that during or soon after the formation of the host DM halo, the baryons falling into the newly created potential well are shock-heated to the virial temperature. The hot gas is (moderately) clumpy and cools quickly in the denser central regions, triggering a strong burst of star formation. The radiation drag due to starlight acts on the gas clouds, reducing their angular momentum. As a consequence, a fraction of the cool gas falls into a reservoir around the central supermassive black hole (BH), and eventually accretes on to it by viscous dissipation, powering the nuclear activity. The energy fed back to the gas by SN explosions and AGN activity regulates the ongoing star formation and the BH growth. Eventually, the SN and the AGN feedbacks unbind most of the gas from the DM potential well. The evolution turns out to be faster in the more massive galaxies, where both the star formation and the BH activity come to an end on a shorter time-scale, due to the QSO feedback whose kinetic power is proportional, according to the model, to  $M_{\text{BH}}^{3/2}$ .

Mao et al. (2007) found that, for the masses and redshifts of interest here, the evolution of the hot (virial temperature) gas mass, taking into account both heating and cooling processes, is well approximated by a simple exponential law

$$M_{\text{hot}}(t) = M_{\text{hot}}(0) e^{-t/t_{\text{cond}}}, \quad (1)$$

where  $M_{\text{hot}}(0) = f_{\text{cosm}} M_{\text{vir}}$  is the gas mass at virialization,  $M_{\text{vir}}$  being the halo mass and  $f_{\text{cosm}} \approx 0.18$  the mean cosmological baryon to DM mass density ratio. The evolution time-scale  $t_{\text{cond}}$  can be approximated as

$$t_{\text{cond}} \approx 4 \times 10^8 \left( \frac{M_{\text{vir}}}{10^{12} M_\odot} \right)^{0.2} \left( \frac{1+z}{7} \right)^{-1.5} \text{ yr}. \quad (2)$$

The model proved to be remarkably successful in accounting for a broad variety of data, including epoch dependent luminosity functions and number counts in different bands of spheroidal galaxies and of AGN, the local BH mass function, metal abundances, fundamental plane relations and relationships between the BH mass and properties of the host galaxies (Silva et al. 2005; Granato et al. 2004; Cirasuolo et al. 2005; Lapi et al. 2006).

<sup>2</sup> <http://www.skatelescope.org/>.

<sup>3</sup> <http://www.alma.info/>.

<sup>4</sup> <http://www.aoc.nrao.edu/evla/>.

## 2.1 The virial collapse

The virial temperature of a uniform spherically symmetric protogalactic cloud with virial mass  $M_{\text{vir}}$  (DM plus baryons) and mean molecular weight  $\mu = (2X + 3/4Y)^{-1}$ ,  $X$  and  $Y$  being the baryon mass fractions in the form of hydrogen and helium (we adopt  $X = 0.75$  and  $Y = 0.25$ , no metals) is

$$T_{\text{vir}} = \frac{1}{2} \frac{\mu m_p G M_{\text{vir}}}{k_B R_{\text{vir}}}, \quad (3)$$

where  $m_p$  is the proton mass,  $G$  the gravitational constant and  $k_B$  the Boltzmann constant. The virial radius  $R_{\text{vir}}$  is given by

$$R_{\text{vir}} = \left( \frac{4}{3} \pi \frac{\rho_{\text{vir}}}{M_{\text{vir}}} \right)^{-1/3}, \quad (4)$$

where  $\rho_{\text{vir}}$  is the mean matter density within  $R_{\text{vir}}$ :

$$\rho_{\text{vir}} = \rho_c \Omega_m \Delta (1+z)^3, \quad (5)$$

$\rho_c = 3H_0^2/(8\pi G)$  being the critical density. For a flat cosmology ( $\Omega_m + \Omega_\Lambda = 1$ ), the virial overdensity  $\Delta$  can be approximated by (Bryan & Norman 1998; Bullock et al. 2001)

$$\Delta = \frac{18\pi^2 + 82\omega - 39\omega^2}{\Omega(z)}, \quad (6)$$

with  $\omega = \Omega(z) - 1$ , and

$$\Omega(z) = \frac{(1+z)^3 \Omega_m}{\Omega_m (1+z)^3 + \Omega_\Lambda}. \quad (7)$$

In the redshift range considered here ( $z \geq 1.5$ ), we have

$$T_{\text{vir}} \simeq 5 \times 10^5 \left( \frac{M_{\text{vir}}}{10^{12} M_\odot} \right)^{2/3} (1+z) \text{ K}, \quad (8)$$

so that for the massive objects ( $2.5 \times 10^{11} < M_{\text{vir}} < 10^{13.2} M_\odot$ ) we are dealing with, the only relevant cooling mechanism is free-free emission.

We assume that, after virialization, the protogalaxy has an NFW density profile (Navarro, Frenk & White 1997):

$$\rho = \frac{\rho_s}{cx(1+cx)^2}, \quad (9)$$

where  $x = r/R_{\text{vir}}$ ,

$$\rho_s = \frac{M_{\text{vir}}}{4\pi R_{\text{vir}}^3 f_c} \quad (10)$$

with

$$f_c = \frac{\log(1+c) - c/(1+c)}{c^3}$$

and  $c = 3$  (Zhao et al. 2003b; Cirasuolo et al. 2005).

## 2.2 The free-free emission

The free-free luminosity of the protogalaxy is computed integrating over its volume the emissivity given by (Rybicki & Lightman 1979):

$$j_{\text{ff}} = 6.8 \times 10^{-38} n_e \left( \sum Z_i^2 n_i \right) C T_{\text{vir}}^{-1/2} \bar{g}_{\text{ff}}(T_{\text{vir}}, \nu) \times \exp(-h_p \nu / k_B T_{\text{vir}}) \text{ erg s}^{-1} \text{ cm}^{-3} \text{ Hz}^{-1}, \quad (11)$$

where the sum in the brackets is on all the chemical species in the gas (only H and He in our case)  $Z$  being the atomic number and  $n_e$  and  $n_i$  the number densities of electrons and of ions respectively,  $C$  is the clumping factor, for which we adopt the value ( $C = 7$ ) given by Lapi et al. (2006),  $h_p$  is the Planck constant and  $\bar{g}_{\text{ff}}(T_{\text{vir}}, \nu)$  is the velocity averaged Gaunt factor. For the latter we adopted

the analytical approximation formulae by Itoh et al. (2000) in their range of validity. Outside such range we used the formula given by Rybicki & Lightman (1979):

$$g_{\text{ff}} = \frac{\sqrt{3}}{\pi} \left[ 17.7 + \ln \left( \frac{T_{\text{vir}}^{3/2}}{\nu} \right) \right]. \quad (12)$$

The gas density is assumed to be proportional to the mass density ( $\rho_{\text{gas}} = f_{\text{cosm}} \rho$ ). The electron number density is

$$n_e = \frac{\rho_{\text{gas}}}{m_p} (X + Y/2), \quad (13)$$

$m_p$  being the proton mass. The adopted value of the clumping factor  $C$  is assumed to be constant with radius, as in the model. This rather crude approximation stems from our ignorance of the complex structure of the gas distribution.

Finally, the flux scales with mass, redshift and frequency as

$$S_{\text{ff}} = 6.6 \times 10^{-9} \bar{g}_{\text{ff}}[T_{\text{vir}}, \nu(1+z)] \left( \frac{1+z}{3} \right)^{7/2} \left( \frac{M_{\text{vir}}}{10^{12} M_\odot} \right)^{2/3} \times \left( \frac{4.8 \times 10^{28} \text{ cm}}{d_L} \right)^2 \exp \left[ \frac{-1.9 \times 10^{-6} (\nu/20 \text{ GHz})}{(M_{\text{vir}}/10^{12} M_\odot)^{2/3}} \right] \text{ Jy}, \quad (14)$$

where  $d_L$  is the luminosity distance (Hogg 1999):

$$d_L = \frac{c}{H_0} (1+z) \int_0^z \frac{dz'}{\sqrt{\Omega_m (1+z')^3 + \Omega_\Lambda}}. \quad (15)$$

## 2.3 The thermal Sunyaev-Zel'dovich effects

The inverse Compton scattering of the cosmic microwave background (CMB) photons by hot electrons produces a distortion of the CMB spectrum, known as SZ effect (Sunyaev & Zel'dovich 1972). The distortion consists in an increase of photon energies which implies a decrease of the CMB brightness temperature at low frequencies ( $\nu < 218 \text{ GHz}$  for  $T_{\text{CMB}} = 2.728 \text{ K}$ ) and an increase at high frequencies:

$$\frac{\Delta T_{\text{CMB}}}{T_{\text{CMB}}} = (x \coth x/2 - 4)y, \quad (16)$$

where  $x = h_p \nu / (k_B T_{\text{CMB}})$  and  $y$  is the comptonization parameter

$$y = \frac{k_B \sigma_T}{m_e c^2} \int dl n_e T_e, \quad (17)$$

$\sigma_T$  being the Thomson cross-section and  $m_e$  the electron mass. In the Rayleigh-Jeans region ( $x \ll 1$ ) equation (16) simplifies to

$$\frac{\Delta T_{\text{CMB}}}{T_{\text{CMB}}} \simeq -2y. \quad (18)$$

The SZ signal corresponds to an unresolved flux

$$S_{\text{ISZ}} = 2 \frac{(k_B T_{\text{CMB}})^3}{(h_p c)^2} g(x) Y, \quad (19)$$

where

$$g(x) = \frac{x^4 \exp(x)}{[\exp(x) - 1]^2} (x \coth x/2 - 4) \quad (20)$$

and  $Y$  is the surface integral of the comptonization parameter.  $S_{\text{ISZ}}$  scales with mass, redshift and frequency as

$$S_{\text{ISZ}} = 0.6 \times 10^{-7} \left( \frac{1+z}{3} \right)^5 \left( \frac{M_{\text{vir}}}{10^{12} M_\odot} \right)^{5/3} \times \left( \frac{4.8 \times 10^{28} \text{ cm}}{d_L} \right)^2 \left[ \frac{g(x)}{0.24} \right] \text{ Jy}, \quad (21)$$

and may be positive or negative depending on the sign of  $g(x)$ . Here we will quote only positive fluxes, taking the absolute value of  $g(x)$ .

For a virialized cloud with  $M_{\text{vir}} \simeq 10^{12} M_{\odot}$  at  $z = 2$ , which has a virial temperature  $T_e \sim 1.4 \times 10^6$  K, a mean electron density  $n_e \simeq 10^{-3} \text{ cm}^{-3}$  and a virial radius of  $\simeq 106$  kpc, the comptonization parameter is  $\simeq 10^{-7}$ , yielding a negative flux of  $\simeq 60$  nJy at 20 GHz, on an angular scale of  $\simeq 10$  arcsec.

## 2.4 The kinetic Sunyaev–Zel’dovich effects

The kSZ effect is due to scattering of CMB photons by an ionized cloud moving with peculiar velocity  $v$ . The associated flux density is (Carlstrom et al. 2002)

$$S_{\text{kSZ}} = -\frac{v_p}{c} 2 \frac{(k_B T_{\text{CMB}})^3}{(h_p c)^2} h(x) \int \tau_e d\Omega, \quad (22)$$

where

$$h(x) = \frac{x^4 \exp(x)}{[\exp(x) - 1]^2}, \quad (23)$$

$\tau_e$  is the optical depth,  $v_p$  is the line-of-sight component of the velocity and the surface integral of  $\tau_e$  is carried out over the solid angle of the moving cloud. The resulting CMB spectrum is still Planckian, but shifted towards higher (lower) temperatures for negative (positive) velocities (where negative means towards the observer). The function  $h(x)$  has a maximum at  $\nu = 218$  GHz where the thermal effect vanishes.  $S_{\text{kSZ}}$  scales as

$$S_{\text{kSZ}} = 5.3 \times 10^{-8} (|v|/393 \text{ km s}^{-1}) [(1+z)/3]^4 \times (M_{\text{vir}}/10^{12} M_{\odot}) (4.8 \times 10^{28} \text{ cm}/d_L)^2 [h(x)/0.12] \text{ Jy}. \quad (24)$$

Following Sheth & Diaferio (2001) we model the distribution function of galaxy peculiar velocities,  $P(v)$ , as a Gaussian core with  $\sigma_v = 680 (1+z)^{-1/2} \text{ km s}^{-1}$ , extending up to  $v_t = 1742 (1+z)^{-1/2} \text{ km s}^{-1}$ , followed by exponential wings cut-off at  $v_{\text{max}} = 3000 (1+z)^{-1/2} \text{ km s}^{-1}$ . Normalizing the integral of  $P(v)$  to unity, we have

$$P(v) dv = 5.86 \times 10^{-4} (1+z)^{1/2} (dv/\text{km s}^{-1}) \times \begin{cases} \exp[-0.5(v/\sigma_v)^2] & \text{for } |v| \leq v_t \\ 2.065 \exp(-2.3|v|/v_0) & \text{for } v_t < |v| \leq v_{\text{max}} \end{cases} \quad (25)$$

where  $v_0 = 1000 (1+z)^{-1/2} \text{ km s}^{-1}$ . The adopted scaling with redshift is that appropriate in the linear regime, when the effect of the cosmological constant can be neglected, as is the case in the  $z$  range of interest here.

## 3 SOURCE COUNTS

The mean differential number counts per steradian are given by

$$\frac{d\mathcal{N}(S)}{d \log S} = \int_{\ln(z_0)}^{\ln(z_1)} d \ln(z) z \frac{dV}{dz} n[L(S, z), z] \frac{d \log L}{d \log S}, \quad (26)$$

where  $n(L, z)$  is the comoving epoch-dependent luminosity function per unit  $d \log L$ ,  $dV/dz$  the comoving volume per unit solid angle:

$$\frac{dV}{dz} = \frac{c}{H_0(1+z)^2} \frac{d_L^2}{\sqrt{\Omega_m(1+z)^3 + \Omega_\Lambda}}. \quad (27)$$

According to our model, for any given  $z$  the free–free luminosity of a protospheroid and its tSZ signal depend only on its virial mass. The luminosity function can then be straightforwardly computed integrating the formation rate of virialized objects,  $d^2N(M_{\text{vir}}, z)/$

$d \log M_{\text{vir}} dt$ , over the duration of the ionized phase and multiplying the result by  $d \log M_{\text{vir}}/d \log L$ . To avoid unnecessary complications we keep the free–free luminosity constant at its initial value over a time,  $t_{\text{ion}}$ , equal to the minimum between  $t_{\text{cond}}$  (equation 2), the expulsion time of the interstellar gas,  $\Delta t_{\text{burst}}$ , determining the end of the star formation burst, and the expansion time-scale, and zero afterwards. This simplifying assumption implies that the evolution of the hot gas mass (equation 1), density, clumping factor and temperature are neglected. It is motivated by our expectation that the effect on the free–free luminosity, hence on the counts, of the moderate decrease of the hot gas mass over the time  $t_{\text{ion}}$  is counterbalanced by an increase of the mean gas density and of the clumping factor, as a consequence of the shocks associated to SN explosions and to the AGN feedback. Also, having neglected the contribution to the counts from the free–free emission at  $t > t_{\text{ion}}$ , partly compensates the possible overestimate due to having neglected the decrease of the gas mass. In any case, a more sophisticated calculation does not appear to be warranted since, as discussed in Sections 4.3 and 4.4, the free–free signal turns out to be too weak to be detectable, being overwhelmed by emissions associated to star formation.

Mao et al. (2007) found that  $\Delta t_{\text{burst}}$  (yr) can be approximated as

$$\Delta t_{\text{burst}} \approx 4 \times 10^8 \left( \frac{1+z}{7} \right)^{-1.5} \times \begin{cases} 1 & \text{for } M_{\text{vir}} \geq 10^{12} M_{\odot} \\ (M_{\text{vir}}/10^{12} M_{\odot})^{-0.15} & \text{for } M_{\text{vir}} < 10^{12} M_{\odot} \end{cases}. \quad (28)$$

The mass function of ionized protospheroids at the redshift  $z$  is then

$$\left( \frac{dN_{\text{ion}}(M_{\text{vir}}, z)}{dM_{\text{vir}}} \right)_{\text{ion}} = \int_{t(z)-t_{\text{ion}}}^{t(z)} dt' \frac{d^2N(M_{\text{vir}}, z)}{dM_{\text{vir}} dt'}. \quad (29)$$

The formation rate of protospheroids is well approximated by the positive term of the derivative of the Sheth & Tormen (1999) mass function,  $(dN(M_{\text{vir}}, z)/dM_{\text{vir}})_{\text{ST}}$  (Lapi et al. 2006):

$$\frac{d^2N(M_{\text{vir}}, z)}{dM_{\text{vir}} dt} = \left[ \frac{a \delta_c(z)}{\sigma^2(M_{\text{vir}})} + \frac{2p}{\delta_c(z)} \frac{\sigma^{2p}(M_{\text{vir}})}{\sigma^{2p}(M_{\text{vir}}) + a^p \delta_c^{2p}(z)} \right] \times \left( \frac{dN(M_{\text{vir}}, z)}{dM_{\text{vir}}} \right)_{\text{ST}} \left| \frac{d\delta_c(z)}{dz} \right|, \quad (30)$$

where  $a = 0.707$ ,  $p = 0.3$ ,  $\delta_c(z)$  is the critical overdensity for the spherical collapse,  $\sigma(M_{\text{vir}})$  is the rms amplitude of initial density fluctuations smoothed on a scale containing a mass  $M_{\text{vir}}$ . In turn, the Sheth & Tormen (1999) mass function is given by

$$\left( \frac{dN(M_{\text{vir}}, z)}{dM_{\text{vir}}} \right)_{\text{ST}} = \frac{\rho}{M_{\text{vir}}^2} \nu f(\nu) \frac{d \ln \nu}{d \ln M_{\text{vir}}}, \quad (31)$$

where  $\rho$  is the average comoving density of the universe,  $\nu = [\delta_c(z)/\sigma_\delta(M_{\text{vir}})]^2$ , and

$$\nu f(\nu) = A [1 + (a\nu)^{-p}] \left( \frac{a\nu}{2} \right)^{1/2} \frac{e^{-a\nu/2}}{\pi^{1/2}}, \quad (32)$$

with  $A = 0.322$ .

The calculations leading to the counts of the tSZ ‘fluxes’ are strictly analogous. In the case of the kSZ effect we need also to take into account the redshift dependent distribution of peculiar velocities, and we have

$$\frac{d\mathcal{N}(S_{\text{kSZ}})}{d \log S_{\text{kSZ}}} = \int_{\ln(z_0)}^{\ln(z_1)} d \ln(z) z \frac{dV}{dz} \int_{\ln(v_{\text{min}})}^{\ln(v_{\text{max}})} d \ln(v) \nu P(v) \times \frac{dN_{\text{ion}}[M_{\text{vir}}(z, v)]}{d \log M_{\text{vir}}} \frac{d \log M_{\text{vir}}}{d \log S_{\text{kSZ}}}, \quad (33)$$

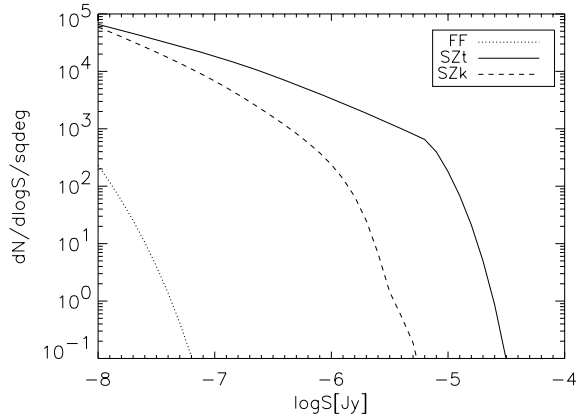


**Figure 1.** Comparison of the differential source counts at 20 GHz of thermal (solid lines) and kinetic (dashed lines) SZ effects and free-free (dotted line). For SZ effects we obviously use the absolute value of the flux. The counts of the kSZ effect include both positive and negative signals, and are therefore a factor of 2 larger than those given by equation (33). The decline of the counts of SZ effects at the faint end is due to the adopted lower redshift ( $z \geq 1.5$ ) and halo mass ( $M_{\text{vir}} \geq 2.5 \times 10^{11} M_{\odot}$ ) limits.

where  $v_{\text{min}}$  is the velocity yielding a kSZ ‘flux’  $S_{\text{kSZ}}$  from a galaxy with the maximum considered mass ( $M_{\text{vir}} = 10^{13.2} M_{\odot}$ ) at redshift  $z$ ,  $dN_{\text{ion}}(M_{\text{vir}}, z, v)/dM_{\text{vir}}$  is the differential mass function of protospheroidal galaxies with peculiar velocity  $v$  and redshift  $z$ , producing a kSZ flux  $S_{\text{kSZ}}$ . As before,  $dN_{\text{ion}}(M_{\text{vir}}, z, v)/dM_{\text{vir}}$  is computed integrating the formation rate of virialized objects over the duration of the ionized phase. Equation (26) gives the number of either positive or negative kSZ signals. The comparison of the differential source counts at 20 GHz in Fig. 1 shows that the tSZ effect is dominant above  $10^{-8}$  Jy. The decline of the SZ counts at faint flux levels is due to the adopted lower limits to halo masses and redshifts ( $M_{\text{vir}} \geq 2.5 \times 10^{11} M_{\odot}$  and  $z \geq 1.5$ ). The very steep slope at the bright end comes from the high halo mass cut-off. The free-free counts are very low, indicating that this emission is very hard to detect in the radio.

As illustrated by Fig. 2, the SZ fluxes increase with increasing frequency in the Rayleigh–Jeans region of the CMB.

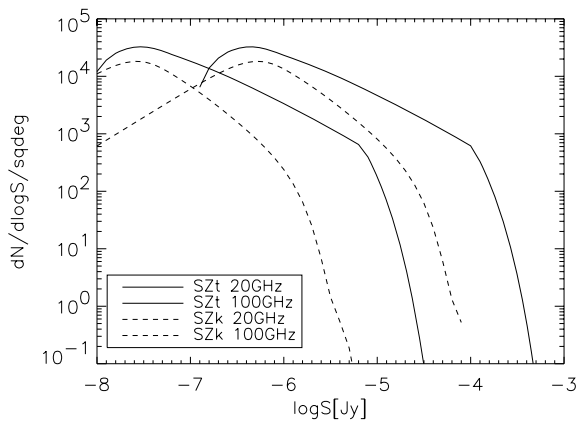


**Figure 2.** Comparison of the differential source counts at 20 and 100 GHz of thermal (thin and thick solid lines respectively) and kinetic (thin and thick dashed lines) SZ effects.

**Table 1.** Main properties of next generation interferometers. The maximum baseline has been calculated considering that the angular size, for the galaxies in the intervals of mass and redshift we are considering, ranges from 5 to 35 arcsec, and requiring a ratio of 5 between amplitude and noise on the visibilities. 10 per cent SKA has the same properties as SKA, but the number of baselines is  $1.25 \times 10^5$ .

	Full SKA	ALMA	ATCA	EVLA
Frequency (GHz)	10–20	100	35–50	35
Bandwidth (GHz)	4	$4 \times 2$	$2 \times 2$	8
Antenna diameter (m)	12 m	12	22	25
Efficiency	0.8	0.8	0.8	0.8
$T_{\text{sys}}$ (K)	50	50	60–80	75
Number of polarizations	2	2	2	2
Minimum baseline (m)	15	15	30.6	30
Maximum baseline (km)	1.4–0.7	0.2	0.4–0.3	0.4
Number of baselines	$1.25 \times 10^7$	700	10	350

## 4 PERSPECTIVES FOR SEARCHES OF IONIZED PROTOSPHEROIDAL CLOUDS

### 4.1 Next generation millimetre-wave interferometers

In Table 1 we have collected some of the main properties of next generation radio interferometers working at few centimetres to millimetres wavelengths.

The ATCA is a six 22-m dish array. The technical parameters we use here refer to the recently completed upgrade to the 7-mm receivers and the increase of the bandwidth from the present  $2 \times 128$  MHz up to 4 GHz (CABBS). The band ranges between 30 and 50 GHz, with  $T_{\text{sys}}$  increasing from 60 to 80 K at the top end of the band. The system will be fully operational by 2008.

The ALMA is a 50 12-m antenna array. The lower frequency band with higher priority ranges between 84 and 116 GHz, close to the maximum amplitude in flux of the negative signal of tSZ effect. The array will be operational by 2012.

The EVLA is an improvement of the sensitivity, frequency coverage and resolution of the existing VLA. When completed, after 2013, it will use the 27 25-m dishes of VLA working in the frequency range between 1–50 GHz with 8-GHz bandwidth per polarization available in the frequency bands 18–26.5, 26.5–40, and 40–50 GHz.

The SKA is a titanic project for an interferometer whose main technical specification is to have at least  $1 \text{ km}^2$  of detecting area in the core region. The highest frequency band should span the range 16–25 GHz. Several designs are under consideration. The parameters we use refer to the small parabolic dishes version, which is the only high-frequency design being considered. The telescope is expected to be fully operational after 2020, but a ‘10 per cent SKA’ is expected to be operating as early as 2015. Phased array feeds in the focal plane are being considered for the lower frequency receivers. If such systems were implemented at the higher frequencies they would increase the field of view (FOV) and hence the survey speed by factors of up to 50.

The angular resolution of an array of antennas is given by

$$\theta = 1.02 \frac{\lambda}{B}, \quad (34)$$

where  $B$  is the maximum distance between two antennas. The FOV normally corresponds to the half-power beam width (HPBW) of an antenna

$$\text{HPBW} = 1.02 \frac{\lambda}{D}, \quad (35)$$

where  $D$  is the diameter of the antenna dish. For a Gaussian beam the FOV is

$$\text{FOV} = \frac{\pi}{\ln 2} \left( \frac{\text{HPBW}}{2} \right)^2. \quad (36)$$

Phased array feedhorns add a multiplying factor to this relation, increasing by the same factor the sky area covered in a single pointing.

The noise level in an image is given by

$$\sigma_{\text{image}} = \frac{k_B T_{\text{sys}}}{A \eta_q \eta} \sqrt{\frac{1}{t N_{\text{base}} \Delta \nu n_{\text{pol}}}}, \quad (37)$$

where  $T_{\text{sys}}$  is the system temperature,  $A$  is the antenna surface area,  $\eta$  is the system (dish and receiver) efficiency,  $t$  is the integration time,  $N_{\text{base}}$  is the number of baselines short enough to have full sensitivity to observe objects with size between 5 and 35 arcsec,  $\Delta \nu$  is the bandwidth and  $n_{\text{pol}}$  is the number of polarizations. Considering the NFW profile for densities enlarges the range of full sensitivity baselines in the visibility space improving the resolution without losing too much in sensitivity. We made our calculations using a reasonably conservative configuration.

Reference values of the quantities used in the calculations for the instruments mentioned above are given in Table 1.

Assuming as detection level of an object emitting flux  $S_{\text{lim}}$  the ratio  $S_{\text{lim}}/\sigma_{\text{image}} = 5$ , for a given telescope the integration time required for each pointing can be obtained by inverting equation (37). The number of pointings necessary to cover a sky area  $A_s$  is

$$n_p = A_s/\text{FOV}. \quad (38)$$

If the integral counts of sources scale as  $S^{-\beta}$ , the number of sources detected in a given area scales as  $t^{\beta/2}$ . For a given flux, the number of detections is proportional to the surveyed area, i.e. to  $t$ . Thus, to maximize the number of detections in a given observing time we need to go deeper if  $\beta > 2$  and to survey a larger area if  $\beta < 2$ . The number of sources detected above a given flux limit,  $S_{\text{lim}}$ , within a telescope FOV,  $N_{\text{FOV}}$ , is straightforwardly derived from the source counts. The number of such pointings necessary to detect  $N_s$  sources is  $n_p = N_s/N_{\text{FOV}}(S_{\text{lim}})$  and the corresponding surveyed area is  $A_s = n_p \text{FOV}$ . The predicted integral counts of tSZ and kSZ effect for several frequencies, covered by the radio interferometers mentioned above, are shown in Figs 3 and 4, respectively. The scale on the right-hand side of these figures gives the corresponding area containing 100 protospheroids.

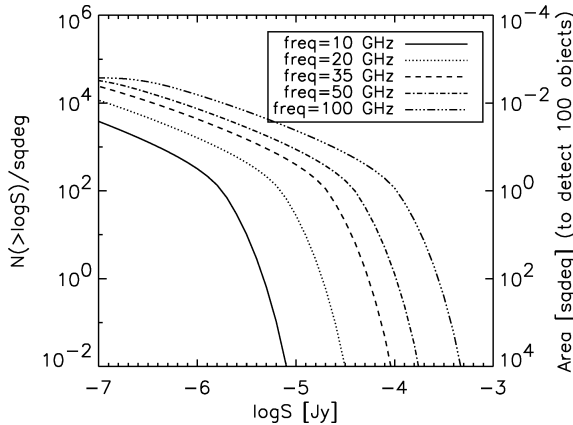


**Figure 3.** Integral counts and sky area required to detect the tSZ effect of 100 protospheroids (right-hand scale) as a function of the absolute value of the ‘flux’ at 20, 35 and 100 GHz.

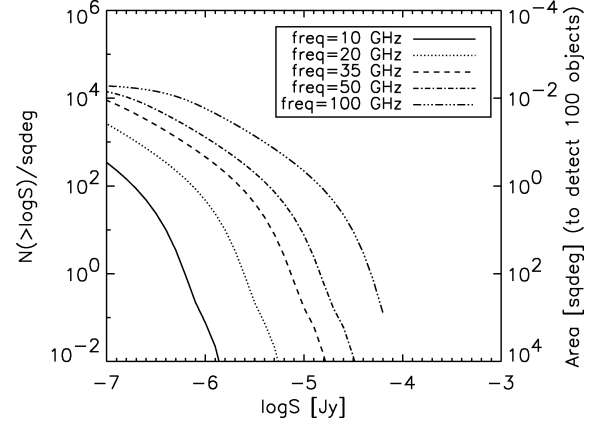


**Figure 4.** Same as Fig. 3, but for the kSZ effect. As in Fig. 1, the counts include both positive and negative signals; for the latter,  $S$  is obviously the absolute value of the flux.

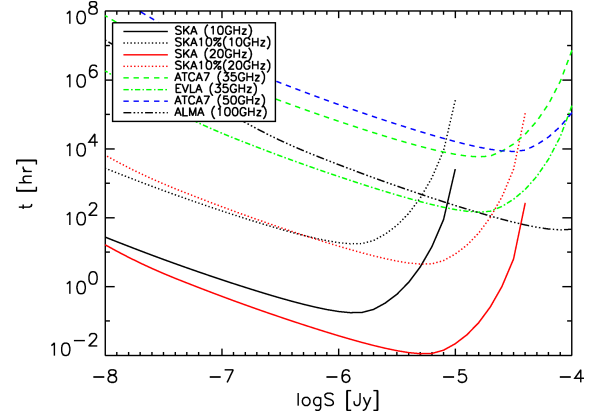


**Figure 5.** Total survey time for ALMA, SKA, EVLA and ATCA to detect 100 protospheroids in tSZ at the frequencies specified in the inset.

The time necessary to reach the wanted  $S_{\text{lim}}$  with  $S/N = 5$  in a single pointing,  $t_p$ , is obtained from equation (37), and the total observing time for detecting  $N_s$  sources (excluding the slew time) is obviously  $t_p n_p$ . In Figs 5 and 6 we show the on-source time  $t_p n_p$  for  $N_s = 100$  as a function of the absolute value of the tSZ and kSZ limiting flux for the four instruments in Table 1 at the frequencies specified in the inset. The curves have minima at the values of  $S_{\text{lim}}$

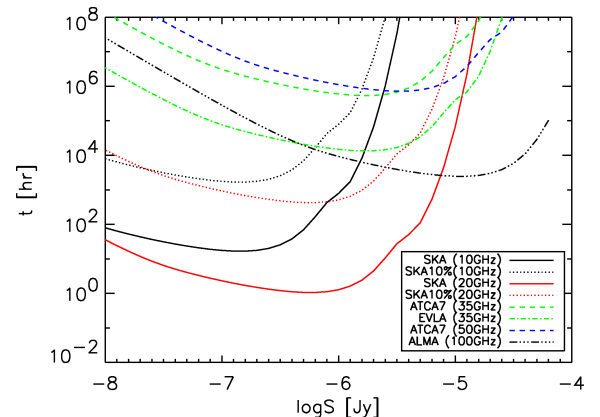


**Figure 6.** Same as Fig. 5, but for the kSZ effect.

corresponding to the fastest survey capable of detecting the wanted number of sources. Clearly, it will be very time consuming to detect 100 protospheroids with the EVLA, and unrealistic with the ATCA. On the other hand, since the 7-mm upgrade of ATCA will be operational already in 2008, it will be possible to exploit it to get the first test of the present predictions, and possibly to achieve the first detection of an SZ signal from a protospheroidal galaxy.

The SKA large effective collecting area allows the detection of tSZ signals of 100 protospheroidal galaxies at 20(10) GHz in 1(11) minutes with 7(7) pointings reaching  $S_{\text{lim}} = 10^{-5.3}$  ( $10^{-5.9}$ ) Jy in a 0.46(0.47) deg<sup>2</sup> area. The 10 per cent SKA requires 100 times more time than the full SKA but is still faster than EVLA or ALMA. If phased array feeds were available at the higher frequencies they would improve these surveying times by a factor of up to 50.

#### 4.2 Redshift distributions

The redshift distributions of tSZ and kSZ effects are illustrated, for three values of  $S_{\text{lim}}$ , in Figs 7 and 8. They are both relatively flat, as the fast decrease with increasing  $z$  of the density of massive (i.e. SZ bright) haloes is partially compensated by the brightening of SZ signals (equations 21 and 24). Such brightening is stronger for the tSZ than for the kSZ. A consequence of such brightening is that the range of halo masses yielding signals above a given limit shrinks with decreasing redshift, as the minimum detectable halo

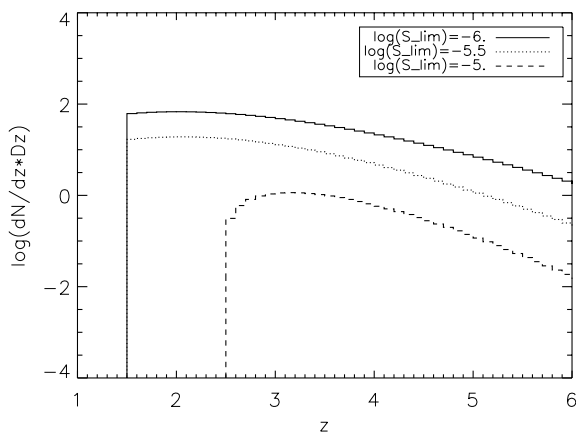


**Figure 7.** Redshift distribution (in bins of width  $\delta z = 0.1$ ) of tSZ effects at 20 GHz for the flux limits specified in the inset.

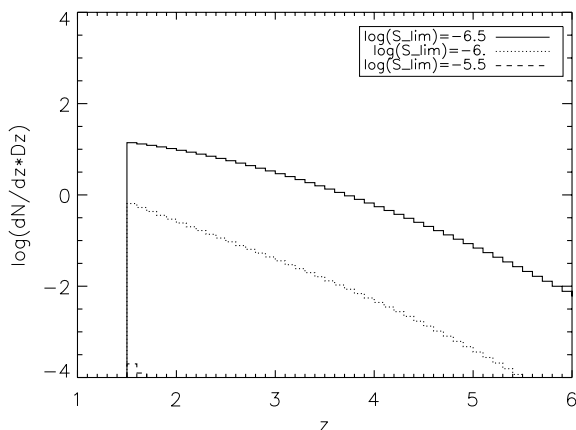


**Figure 8.** Same as in Fig. 7, but for the kSZ effect.

mass increases. The upper limit on masses of galactic haloes then translates in a lower limit to the redshift distribution for bright  $S_{\text{lim}}$ .

#### 4.3 Contaminant emissions

The adopted model envisages that the plasma halo has the same size as the DM halo, i.e. of the order of hundreds of kpc. In the central region (with size of the order of 10 kpc), the gas cools rapidly and forms stars. Bressan, Silva & Granato (2002) obtained a relationship between the star formation rate (SFR) and the radio luminosity at 8.4 GHz,  $L_S(8.4 \text{ GHz})$ :

$$L_S(8.4 \text{ GHz}) \simeq 3.6 \times 10^{27} \frac{\text{SFR}}{M_{\odot} \text{ yr}^{-1}} \text{ erg s}^{-1} \text{ Hz}^{-1}. \quad (39)$$

This relationship is in good agreement with the estimate by Carilli (2001) while the equations in Condon (1992) imply a radio luminosity about a factor of 2 lower, at fixed SFR. The Granato et al. (2004) model gives the SFR as a function of galactic age,  $t_{\text{gal}}$ , for any value of the halo mass and of the virialization redshift (see e.g. fig. 1 of Mao et al. 2007). We must, however, take into account that equation (39) has been derived using a Salpeter (1955) initial mass function (IMF). For the IMF used by Granato et al. (2004), the radio luminosity associated to a given SFR is higher by a factor of 1.6 (Bressan, personal communication). The coefficient in equation (39) was therefore increased by this factor.

The mean rest frame 8.4-GHz luminosity at given  $M_{\text{vir}}$  and  $z_{\text{vir}}$  was then obtained using the corresponding SFR averaged over  $t_{\text{gal}}$  in the renormalized equation (39). Extrapolations in frequency have been obtained using, as a template, the fit to the Arp 220 continuum spectrum obtained by Bressan et al. (2002; solid line in their fig. 2). Using the continuum spectrum of M 82 (solid line in fig. 1 of Bressan et al.), the other standard starburst template, we get essentially identical results.

In Fig. 9 we compare the flux associated with star formation with the tSZ ‘flux’ (equation 21), as a function of the virialization redshift, for several values of  $M_{\text{vir}}$ . For a given halo mass, the ratio of the tSZ to the contaminating signal increases with frequency (and with redshift) as far as the contamination is due to radio emission associated to star formation (we do not consider here nuclear radio emission, which occurs in  $\lesssim 10$  per cent of galaxies). However, already at 20 GHz the thermal dust emission becomes important for the highest redshift sources. Such emission is more steeply

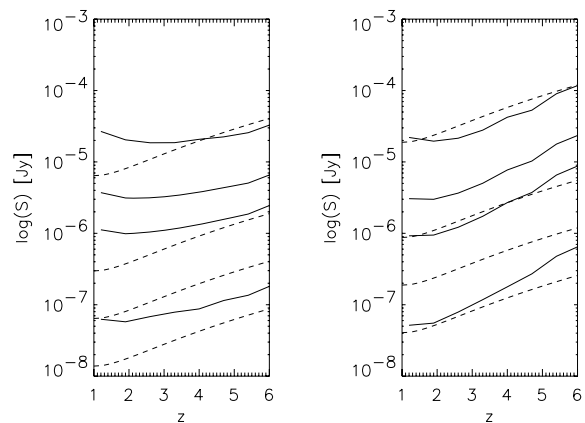


**Figure 9.** Comparison of the flux associated with star formation (solid lines) with the tSZ ‘flux’ (dashed lines) at 20 GHz (left-hand panel) and at 35 GHz (right-hand panel), as a function of the virialization redshift for four values of the virial mass [ $\log(M_{\text{vir}}) = 11.5, 12., 12.5, 13.2$ , from bottom to top].

increasing with frequency than the SZ signal, even in the Rayleigh–Jeans region of the CMB, and rapidly overwhelms it at  $\gtrsim 100$  GHz. The SZ/contamination ratio increases with increasing halo mass; therefore the SZ detection is easier for the more massive haloes. Thus in the range 10–35 GHz the tSZ is expected to dominate over the contaminating signal at least for the most massive objects.

It must be noted that the star-forming regions are concentrated in the core of the spheroids, on angular scales of the order of or less than 1 arcsec, for the redshifts considered here. Long ( $\gtrsim 3$  km at 35 GHz for full sensitivity) baselines observation with high sensitivity may be able to resolve the star-forming region positive signal and subtract it from the image. To achieve this purpose a good sampling of the shortest spacings on the  $uv$  plane is necessary together with a good sampling of the largest ones: with the latter it might be possible to reconstruct the contaminated profile, subtract it from the former and produce an uncontaminated SZ profile. Again, the SKA at high frequencies seems to be the optimal instrument.

#### 4.4 Confusion effects

Further constraints to the detection of SZ effects are set by confusion fluctuations. Fomalont et al. (2002) have determined the 8.4-GHz source counts down to  $7.5 \mu\text{Jy}$ . For  $S_{8.4\text{GHz}} \lesssim 1$  mJy they are well described by

$$N(> S) \simeq 1.65 \times 10^{-3} S^{-1.11} \text{ arcsec}^{-2} \quad (40)$$

with  $S$  in  $\mu\text{Jy}$ . The spectral index distribution peaks at  $\alpha \simeq 0.75$  ( $S \propto \nu^{-\alpha}$ ).

For all but one (SKA 10 GHz) of the considered surveys the ‘optimal’ depth for detecting 100 sources corresponds to 8.4-GHz flux densities within the range covered by Fomalont et al. (2002), so that the confusion fluctuations are dominated by sources obeying equation (40). We then have

$$\sigma_{\text{conf}}^2 \simeq 0.2 \left( \frac{\nu}{8 \text{ GHz}} \right)^{-1.11\alpha} \frac{\omega}{100 \text{ arcsec}^2} S_{\text{d}}^{0.89} \mu\text{Jy}^2, \quad (41)$$

where  $S_{\text{d}}$ , in  $\mu\text{Jy}$ , is the detection limit and  $\omega$  is the solid angle subtended by the SZ signal. Equation (41) can be rewritten as

$$\frac{S_{\text{d}}}{\sigma_{\text{conf}}} \simeq 2.2 \left( \frac{\nu}{8.4 \text{ GHz}} \right)^{0.555\alpha} \left( \frac{\omega}{100 \text{ arcsec}^2} \right)^{-1/2} S_{\text{d},10\mu\text{Jy}}^{0.555}, \quad (42)$$

yielding a  $5\sigma_{\text{conf}}$  detection limit of  $\simeq 4 \mu\text{Jy}$  at 10 GHz and of  $\simeq 2.3 \mu\text{Jy}$  at 20 GHz. For the ‘optimal’ survey depths at higher frequencies  $S_{\text{d}}/\sigma_{\text{conf}} \gg 5$ , implying that they are not affected by confusion noise due to radio sources.

On the other hand, as noted above, at high frequencies the redshifted dust emission from distant star-forming galaxies becomes increasingly important (de Zotti et al. 2005). To estimate their contribution to the confusion noise, we have used once again the model by Granato et al. (2004), with the dust emission spectra revised to yield  $850\mu$  counts consistent with the results by Coppin et al. (2006), and complemented by the phenomenological estimates by Silva et al. (2005) of the counts of sources other than high- $z$  protospheroids (see Negrello et al. (2007) for further details). We find, for a typical solid angle  $\omega = 100 \text{ arcsec}^2$ ,  $5\sigma_{\text{conf}}$  flux limits due to these sources of 3, 55 and  $190 \mu\text{Jy}$  at 20, 35 and 50 GHz, respectively. Thus at 20 GHz we have significant contributions to the confusion noise both from the radio and from the dust emission; the overall  $5\sigma_{\text{conf}}$  detection limit is  $S_{\text{d}} \simeq 4 \mu\text{Jy}$ . At 10 GHz the contribution of dusty galaxies to the confusion noise is negligible, while at 100 GHz the confusion limit is as high as 2 mJy, implying that the detection of the galactic-scale SZ effect is hopeless at millimetre wavelengths.

Although high- $z$  luminous star-forming galaxies may be highly clustered (Blain et al. 2005; Farrah et al. 2006; Magliocchetti et al. 2007), the clustering contribution to fluctuations is negligible on the small scales of interest here (de Zotti et al. 1996), and can safely be neglected.

## 5 CONCLUSIONS

In the standard scenario for galaxy formation, the protogalactic gas is shock heated to the virial temperature. The observational evidences that massive star formation activity must await the collapse of large haloes, a phenomenon referred to as *downsizing*, suggest that protogalaxies with a high thermal energy content existed at high redshifts. Such objects are potentially observable through the tSZ and kSZ effects and their free–free emission. The detection of this phase of galaxy evolution would shed light on the physical processes that govern the collapse of primordial density perturbations on galactic scales and on the history of the baryon content of galaxies.

As for the latter issue, the standard scenario, adopted here, envisages that the baryon to DM mass ratio at virialization has the cosmic value, i.e. is about an order of magnitude higher than in present-day galaxies. Measurements of the SZ effect will provide a direct test of this as yet unproven assumption, and will constrain the epoch when most of the initial baryons are swept out of the galaxies.

As mentioned in Section 1, almost all semi-analytic models for galaxy formation adopt halo mass functions directly derived or broadly consistent with the results of  $N$ -body simulations, and it is commonly assumed that the gas is shock heated to the virial temperature of the halo. They therefore entail predictions on counts of SZ effects similar to those presented here. On the other hand, the thermal history of the gas is governed by a complex interplay of many astrophysical processes, including gas cooling, star formation, feedback from SNe and active nuclei, shocks. As mentioned in Section 1, recent investigations have highlighted that a substantial fraction of the gas in galaxies may not be heated to the virial temperature. Also, it is plausible that the AGN feedback transiently heats the gas to temperatures substantially above the virial value, thus yielding SZ signals exceeding those considered here. The gas thermal history may therefore be substantially different from that envisaged by semi-analytic models, and the SZ observations may provide unique information on it.

We have presented a quantitative investigation of the counts of SZ and free–free signals in the framework of the Granato et al. (2004) model, that successfully accounts for the wealth of data on the cosmological evolution of spheroidal galaxies and of AGN (Granato et al. 2004; Cirasuolo et al. 2005; Silva et al. 2005; Lapi et al. 2006).

We find that the detection of substantial numbers of galaxy-scale tSZ signals is achievable by blind surveys with next generation radio interferometers. Since the protogalaxy thermal energy content increases, for given halo mass, with the virialization redshift, the SZ ‘fluxes’ increase rather strongly with  $z$ , especially for the tSZ effect, partially compensating for the rapid decrease of the density of massive haloes with increasing redshift. The redshift distributions of tSZ sources are thus expected to have substantial tails up to high  $z$ .

There are however important observational constraints that need to be taken into account. The contamination by radio and dust emissions associated to the star formation activity depends on mass and redshift of the objects, but is expected to be stronger than the SZ signal at very low and very high frequencies. We conclude that the optimal frequency range for detecting the SZ signal is from 10 to 35 GHz, where such signal dominates over the contamination at



least for the most massive objects. It must be noted however that contaminating emissions have typical scales of the order of those of the stellar distributions, i.e.  $< 1$  arcsec at the redshifts of interest here (see Fomalont et al. 2006), while the SZ effects show up on the scale of the DM halo, which is typically ten times larger. Therefore arcsec resolution images, such as those that will be provided by the SKA, will allow us to reconstruct the uncontaminated SZ signal.

The coexistence of the hot plasma halo, responsible for the SZ signal, with dust emission implies that the scenario presented in this paper may be tested by means of pointed observations of high- $z$  luminous star-forming galaxies detected by (sub)millimetre surveys.

Confusion noise is a very serious limiting factor at millimetre wavelengths. Contributions to confusion come on one side from radio sources and on the other side from dusty galaxies. At 10 GHz only radio sources matter; a modest extrapolation of the 8.4-GHz  $\mu\text{Jy}$  counts by Fomalont et al. (2002) gives a  $5\sigma_{\text{conf}}$  detection limit  $S_d \simeq 4 \mu\text{Jy}$ , for an SZ signal subtending a typical solid angle of  $100 \text{ arcsec}^2$ . Fluctuations due to dust emission from high- $z$  luminous star-forming galaxies may start becoming important already at 20 GHz; at this frequency, quadratically summing them with those due to radio sources we find again  $S_d \simeq 4 \mu\text{Jy}$ , for the same solid angle. On the other hand, the high resolution of the SKA will allow us to effectively detect and subtract out confusing sources, thus substantially decreasing the confusion effects. Beating confusion will be particularly important for searches of the weaker kSZ signal.

## ACKNOWLEDGMENTS

We are indebted to G. L. Granato for having provided the software to compute the cooling function and the halo mass function, A. Diaferio for explanations on the halo velocity function and its cosmological evolution and A. Bressan for clarifications on the dependence of the radio luminosity/SFR relation on the IMF. We thank M. Rupen for updated information about the EVLA capabilities.

We also warmly thank the anonymous referee for an unusually accurate reading of the manuscript and for many constructive comments.

Work supported in part by the Ministero dell'Università e della Ricerca and by ASI (contract Planck LFI Activity of Phase E2).

## REFERENCES

- Benson A. J., Bower R. G., Frenk C. S., Lacey C. G., Baugh C. M., Cole S., 2003, *ApJ*, 599, 38
- Binney J., 2004, *MNRAS*, 347, 1093
- Birkinshaw M., Lancaster K., 2005, in Melchiorri F., Rephaeli Y., eds, *Proc. Int. School Phys. 'Enrico Fermi', Background Microwave Radiation and Intracluster Cosmology*. IOS Press, The Netherlands and Società Italiana di Fisica, Bologna, p. 127
- Birboim Y., Dekel A., 2003, *MNRAS*, 345, 349
- Blain A. W., Chapman S. C., Smail I., Ivison R., 2005, in Renzini A., Bender R., eds, *Proc. ESO Workshop, Multiwavelength Mapping of Galaxy Formation and Evolution*. Springer, Berlin, p. 94
- Bower R. G., Benson A. J., Malbon R., Helly J. C., Frenk C. S., Baugh C. M., Cole S., Lacey C. G., 2006, *MNRAS*, 370, 645
- Bressan A., Silva L., Granato G. L., 2002, *A&A*, 392, 377
- Bryan G. L., Norman M. L., 1998, *ApJ*, 495, 80
- Bullock J. S., Kolatt T. S., Sigad Y., Somerville R. S., Kravtsov A. V., Klypin A. A., Primack J. R., Dekel A., 2001, *MNRAS*, 321, 559
- Carilli C. L., 2001, in Tacconi L., Lutz D., eds, *Starburst Galaxies: Near and Far*. Springer-Verlag, Heidelberg, p. 309
- Carlstrom J. E., Holder G. P., Reese E. D., 2002, *ARA&A*, 40, 643
- Cirasuolo M., Shankar F., Granato G. L., De Zotti G., Danese L., 2005, *ApJ*, 629, 816
- Cole S., 1991, *ApJ*, 367, 45
- Cole S., Aragon-Salamanca A., Frenk C. S., Navarro J. F., Zepf S. E., 1994, *MNRAS*, 271, 781
- Condon J. J., 1992, *ARA&A*, 30, 575
- Coppin K. et al., 2006, *MNRAS*, 372, 1621
- Croton D. J. et al., 2006, *MNRAS*, 365, 11
- Dekel A., Birboim Y., 2006, *MNRAS*, 368, 2
- Dekel A., Silk J., 1986, *ApJ*, 303, 39
- de Zotti G., Franceschini A., Toffolatti L., Mazzei P., Danese L., 1996, *Astrophys. Lett. and Communications*, 35, 289
- de Zotti G., Burigana C., Cavaliere A., Danese L., Granato G. L., Lapi A., Platania P., Silva L., 2004, in Bertin G., Farina D., eds, *AIP Conf. Proc. Vol. 703, Plasmas in the Laboratory and in the Universe: New Insights and New Challenges*. Am. Inst. Phys., New York, p. 375
- de Zotti G., Ricci R., Mesa D., Silva L., Mazzotta P., Toffolatti L., González-Nuevo J., 2005, *A&A*, 431, 893
- Farrah D. et al., 2006, *ApJ*, 641, L17 (erratum: 2006, *ApJ*, 643, L139)
- Fomalont E. B., Kellermann K. I., Partridge R. B., Windhorst R. A., Richards E. A., 2002, *AJ*, 123, 2402
- Fomalont E. B., Kellermann K. I., Cowie L. L., Capak P., Barger A. J., Partridge R. B., Windhorst R. A., Richards E. A., 2006, *ApJS*, 167, 103
- Granato G. L., Silva L., Monaco P., Panuzzo P., Salucci P., De Zotti G., Danese L., 2001, *MNRAS*, 324, 757
- Granato G. L., De Zotti G., Silva L., Bressan A., Danese L., 2004, *ApJ*, 600, 580
- Haehnelt M. G., Rees M. J., 1993, *MNRAS*, 263, 168
- Hogg D. W., 1999, preprint (arXiv:astro-ph/9905116)
- Itoh N., Sakamoto T., Kusano S., Nozawa S., Kohyama Y., 2000, *ApJS*, 128, 125
- Katz N., Kereš D., Davé R., Weinberg D. H., 2003, in Rosenberg J. L., Putman M. E., eds, *The IGM/Galaxy Connection: The Distribution of Baryons at  $z = 0$* . Kluwer, Dordrecht, p. 185
- Kauffmann G., White S. D. M., Guiderdoni B., 1993, *MNRAS*, 264, 201
- Kereš D., Katz N., Weinberg D. H., Davé R., 2005, *MNRAS*, 363, 2
- Koopmans L. V. E., Treu T., Bolton A. S., Burles S., Moustakas L. A., 2006, *ApJ*, 649, 599
- Lacey C., Silk J., 1991, *ApJ*, 381, 14
- Lapi A., Shankar F., Mao J., Granato G. L., Silva L., De Zotti G., Danese L., 2006, *ApJ*, 650, 42
- Larson R. B., 1974, *MNRAS*, 169, 229
- Magliocchetti M., Silva L., Lapi A., De Zotti G., Granato G. L., Fadda D., Danese L., 2007, *MNRAS*, 375, 1121
- Majumdar S., Nath B. B., Chiba M., 2001, *MNRAS*, 324, 537 (erratum: 2001, *MNRAS*, 326, 1216)
- Mao J., Lapi A., Granato G. L., de Zotti G., Danese L., 2007, *ApJ*, 667, 655
- Navarro J. F., Frenk C. S., White S. D. M., 1997, *ApJ*, 490, 493
- Negrello M., Perrotta F., González J. G.-N., Silva L., de Zotti G., Granato G. L., Baccigalupi C., Danese L., 2007, *MNRAS*, 323
- Oh S. P., 1999, *ApJ*, 527, 16
- Oh S. P., Cooray A., Kamionkowski M., 2003, *MNRAS*, 342, L20
- Platania P., Burigana C., De Zotti G., Lazzaro E., Bersanelli M., 2002, *MNRAS*, 337, 242
- Rees M. J., Ostriker J. P., 1977, *MNRAS*, 179, 541
- Renzini A., 2006, *ARA&A*, 44, 141
- Rybicki G. B., Lightman A. P., 1979, *Radiative Processes in Astrophysics*. Wiley, New York
- Rosa-González D., Terlevich R., Terlevich E., Friaça A., Gaztañaga E., 2004, *MNRAS*, 348, 669
- Salpeter E. E., 1955, *ApJ*, 121, 161
- Sasaki S., 1994, *PASJ*, 46, 427
- Sheth R. K., Tormen G., 1999, *MNRAS*, 308, 119
- Sheth R. K., Diaferio A., 2001, *MNRAS*, 322, 901
- Silva L., Granato G. L., Bressan A., Danese L., 1998, *ApJ*, 509, 103
- Silva L., De Zotti G., Granato G. L., Maiolino R., Danese L., 2005, *MNRAS*, 357, 1295

Somerville R. S., Primack J. R., 1999, MNRAS, 310, 1087  
Spergel D. N. et al., 2007, ApJS, 170, 377  
Sunyaev R. A., Zel'dovich Y. B., 1972, Comments on Astrophys. and Space  
Phys., 4, 173  
Thomas D., Maraston C., Bender R., 2002, Rev. Modern Astron., 15, 219  
Wechsler R. H., Bullock J. S., Primack J. R., Kravtsov A. V., Dekel A., 2002,  
ApJ, 568, 52

White S. D. M., Frenk C. S., 1991, ApJ, 379, 52  
White S. D. M., Rees M. J., 1978, MNRAS, 183, 341  
Zhao D. H., Mo H. J., Jing Y. P., Börner G., 2003a, MNRAS, 339, 12  
Zhao D. H., Jing Y. P., Mo H. J., Börner G., 2003b, ApJ, 597, L9

This paper has been typeset from a  $\text{\TeX/L\AA\TeX}$  file prepared by the author.